

CLUSTER LENSING PROFILES DERIVED FROM A REDSHIFT ENHANCEMENT  
OF MAGNIFIED BOSS-SURVEY GALAXIES

JEAN COUPON

Institute of Astronomy and Astrophysics, Academia Sinica,  
P.O. Box 23-141, Taipei 10617, TaiwanTOM BROADHURST<sup>1</sup>Department of Theoretical Physics, University of Basque Country  
UPV/EHU, P.O. Box 644, E-48080 Bilbao, Spain and  
IKERBASQUE, Basque Foundation for Science, Alameda Urquijo 36-5, E-48008 Bilbao, Spain

AND

KEIICHI UMETSU

Institute of Astronomy and Astrophysics, Academia Sinica,  
P.O. Box 23-141, Taipei 10617, Taiwan*Draft version September 29, 2018*

## ABSTRACT

We report the first detection of a redshift-depth enhancement of background galaxies magnified by foreground clusters. Using 300 000 BOSS-Survey galaxies with accurate spectroscopic redshifts, we measure their mean redshift depth behind four large samples of optically selected clusters from the SDSS surveys, totalling 5 000 – 15 000 clusters. A clear trend of increasing mean redshift towards the cluster centers is found, averaged over each of the four cluster samples. In addition we find similar but noisier behaviour for an independent X-ray sample of 158 clusters lying in the foreground of the current BOSS sky area. By adopting the mass-richness relationships appropriate for each survey we compare our results with theoretical predictions for each of the four SDSS cluster catalogs. The radial form of this redshift enhancement is well fitted by a richness-to-mass weighted composite Navarro-Frenk-White profile with an effective mass ranging between  $M_{200} \sim 1.4\text{--}1.8 \times 10^{14} M_{\odot}$  for the optically detected cluster samples, and  $M_{200} \sim 5.0 \times 10^{14} M_{\odot}$  for the X-ray sample. This lensing detection helps to establish the credibility of these SDSS cluster surveys, and provides a normalization for their respective mass-richness relations. In the context of the upcoming bigBOSS, Subaru-PFS, and EUCLID-NISP spectroscopic surveys, this method represents an independent means of deriving the masses of cluster samples for examining the cosmological evolution, and provides a relatively clean consistency check of weak-lensing measurements, free from the systematic limitations of shear calibration.

*Keywords:* galaxies: clusters: general — gravitational lensing: weak — cosmology: observations — dark matter

## 1. INTRODUCTION

Our current paradigm predicts that the properties of dark energy will be imprinted in the matter power spectrum and its time evolution. Although probing the large scale structure in the universe is a promising strategy to investigate the different dark-energy model candidates, it is becoming increasingly challenging to detect the relatively subtle signatures of the various lesser ingredients and higher order effects, forcing us to observe many independent physical phenomena over gigantic volumes, to reach sufficient joint statistical precision.

In the era of large scale cosmological surveys, gravitational lensing is one of the most promising methods for establishing the fluctuations of matter in the universe, as lensing is purely gravitational and can be largely assumed to be independent of the unknown nature of the dark matter. One may employ two-dimensional (Kilbinger et al. 2013) or tomographic (Benjamin et al.

2012) *cosmic shear* to measure the integrated lensing effect of matter fluctuations along the line-of-sight up to very large scales (Taylor et al. 2004; Massey et al. 2007). Or, one may use cluster abundances (Roza et al. 2010) to put constraints on the evolution of the dark matter halo mass function, which is known to be a very sensitive function of the evolution of the mean mass density and of the dark energy properties. Masses can be derived from the radial shear profile around clusters in the weak lensing regime (Sheldon et al. 2009; Leauthaud et al. 2010; Oguri & Hamana 2011; Umetsu et al. 2012), from X-ray (Rykoff et al. 2008), SZ effect (Marriage et al. 2011), or satellite kinematics (More et al. 2011).

Even though lensing from stacked clusters undoubtedly leads to a less noisy mass estimate among all these methods, accurate statistics will be limited, however, by our ability to measure galaxy shapes down to the required precision. Recently, Heymans et al. (2012) demonstrated that for a survey like the CFHTLS-wide, spreading over  $154 \text{ deg}^2$ , the level of systematics in shape measurement, as given by the state-of-the-art shape measurement technique (Lensfit, Miller et al. 2013), was lower than sta-

coupon@asiaa.sinica.edu.tw

<sup>1</sup> Institute of Astronomy and Astrophysics, Academia Sinica,  
P.O. Box 23-141, Taipei 10617, Taiwan

tistical errors. For upcoming experiments such as the Hyper Suprime Cam (HSC, Miyazaki et al. 2012) survey, the Dark Energy Survey (DES<sup>2</sup>), the Large Synoptic Survey Telescope project (LSST<sup>3</sup>) or EUCLID<sup>4</sup> survey (Laureijs et al. 2011) which will probe volumes orders of magnitude larger than the CFHTLS-wide, the limiting requirements will be much more stringent.

Lens magnification provides independent observational alternatives and complementary means to weak shape measurement (Van Waerbeke et al. 2010; Hildebrandt et al. 2011). In practice magnification bias has been used to improve the mass profiles of individual massive clusters, and stacked samples of clusters from recent dedicated cluster surveys. Here the number counts of flux limited samples of background sources is reduced in surface density by the magnified sky area, and compensated to some extent by fainter objects magnified above the flux limit (Broadhurst et al. 1995, hereafter BTP95) with a net magnification-bias in the surface density depending on the slope of the background counts. For very red background galaxies behind clusters the net effect is a clear “depletion” of red background galaxies towards the cluster center (Broadhurst et al. 2005, 2008) and is used in combination with weak shear to enhance the precision of individual cluster mass profiles (Umetsu & Broadhurst 2008; Umetsu et al. 2011b). A strength of this method resides in the fact that no shape information is used and is therefore less prone to systematic errors, as opposed to shear measurement for which complex corrections are required (Kaiser et al. 1995; Umetsu & Broadhurst 2008).

In the statistical regime, for deep wide area surveys, progress has been made recently in a similar way using distant Lyman-break galaxies behind stacked samples of foreground clusters, resulting in a claimed positive magnification-bias enhancement of the observable surface density of background galaxies at small radius. In practice, some cross contamination of cluster members and foreground galaxies with the background will complicate such measurements. Until recently, magnification bias studies (Ford et al. 2012; Hildebrandt et al. 2013) have faced such a high statistical error that their conclusions were not affected by these systematics. However in the future a careful treatment of potential sources of systematics will be mandatory.

With redshift information for large samples of background galaxies, cluster magnification may be tackled more fully, as the luminosity function of background galaxies is magnified both in the density and luminosity directions, in a characteristic redshift dependent way. For flux limited redshift samples, the redshift distribution becomes skewed to higher mean redshift as a consequence of magnification, and the mean luminosity is also modified owing to the curvature (non-power law) of the luminosity function (BTP95). The latter effect has been claimed in the case of magnified QSO’s behind galaxies in the SDSS survey (Ménard et al. 2010).

In this paper, we are interested in the enhanced redshift depth of background galaxies magnified by foreground clusters and averaged over large cluster samples

recently identified within the SDSS survey. We measure the mean redshift of BOSS galaxies behind SDSS clusters (York et al. 2000; Schlegel et al. 2009; Dawson et al. 2013), using four different catalogues of optically detected clusters found from very different independent methods, including the maxBCG (Koester et al. 2007), the GMBCG (Hao et al. 2010), the Szabo et al. (2011) and the Wen et al. (2012) samples. We compare the depth magnification to the expected lensing signal using mass-richness relationships calibrated from X-ray and weak shear measurements. In addition we use the MCXC X-ray cluster sample assembled by Piffaretti et al. (2011) from a number of independent ROSAT observations.

In Section §2 we present the data sets used in this study; the BOSS sample, the four galaxy cluster catalogs and the X-ray sample. In a third section, we describe our model, and in a fourth section we present our measurement technique, followed by our results presented and discussed in Section §5. In Section §6 we present a brief error analysis and we conclude in Section §7. Everywhere we assume a flat  $\Lambda$ CDM cosmology with  $\Omega_m = 0.258$ ,  $\Omega_\lambda = 0.742$ , and  $h_{100} = 0.72$  (Hinshaw et al. 2009). All masses are expressed in unit of  $M_\odot$ .

## 2. DATA

### 2.1. The lens samples

The Sloan Digital Sky Survey (SDSS, York et al. 2000) is an optical (*ugriz* filters) photometric and spectroscopic survey which represents the largest probe of the local universe to date. In addition to its unprecedented volume observed, the success of the SDSS project is based upon an accurate photometric calibration, an ingenious synergy between photometric and spectroscopic observing strategies, and a handy and well documented database. In the published literature, several methods have been used to construct cluster samples from the SDSS database. In this study, we thus focus on the following four publicly-available cluster catalogs based on optical identifications.

First, the maxBCG cluster catalog (Koester et al. 2007) is a cluster sample constructed from 7500 deg<sup>2</sup> of photometric data in the SDSS. To detect candidate clusters, the method identifies a local overdensity of cluster members along the *red-sequence*. The *richness*  $N_{200}$  is defined as the number of galaxy members which are brighter than  $0.4L_\star$  and lying on the red-sequence inside the radius of  $r_{200}$ , within which the mean interior density is 200 times the critical density of the universe. The public maxBCG catalog consists of cluster candidates with 10 members or more. Since the maxBCG sample was constructed from an earlier SDSS data release, the probed area does not fully overlap with the final SDSS coverage in the Galactic south cap, where BOSS galaxies have been targeted. Therefore, not all of the 3000 deg<sup>2</sup> of BOSS data available to date overlap with the maxBCG cluster sample. Keeping all galaxy-cluster pairs within one deg, the subsample used in this study includes 6308 clusters.

Second, more recently, Hao et al. (2010) proposed a slightly different optical-based detection method, the Gaussian Mixture Brightest Cluster Galaxy (GMBCG), which relies on both the presence of the brightest cluster galaxy (BCG) and the red-sequence to identify clusters.

<sup>2</sup> <http://www.darkenergysurvey.org>

<sup>3</sup> <http://www.lsst.org/>

<sup>4</sup> <http://www.euclid-ec.org/>

Among the differences with maxBCG cluster algorithm finder is the way to estimate the cluster redshift, where for GMBCG it is estimated solely from the BCG photometric redshift (or spectroscopic redshift when available). It is claimed by Hao et al. (2010) that the GMBCG catalog is volume limited out to  $z = 0.4$ ; however, to ensure no spurious correlation between false cluster detection and background sources, secure foreground-background sample separation is necessary. For this reason we limit the GMBCG sample to the range  $0.1 < z < 0.3$ , taking into account the typical photometric redshift error. This redshift selection, in conjunction with rejection of clusters lying outside the BOSS area, leads to a total of 4631 clusters with richness  $N_{200}$  greater than 10. Although an improved *weighted* richness estimator is available, we employ the scaled richness estimator, which is defined in the same way as for the maxBCG catalog.

Third, an alternative method of Dong et al. (2008) does not rely on the red-sequence, but on the peak locations in the likelihood map generated from the convolution of the galaxy distribution in redshift space with aperture matched filters. These filters are constructed from the assumed cluster density profile and galaxy luminosity functions. This method has been applied to the SDSS (Szabo et al. 2011), and the overlap with BOSS allows us to use 5646 galaxy clusters below redshift 0.3. A noticeable feature of this catalog is that the richness is computed as the sum of the luminosity of all galaxies above  $0.4L_*$  divided by  $L_*$ , and is therefore not directly comparable to the definition used by the two previous data samples. The publicly available version includes all clusters with an estimated richness  $\Lambda_{200}$  of 20 or higher. In the rest of the paper, we will refer to this sample as “AMF”.

Fourth, we use the catalog produced by Wen et al. (2012). In this method, a friend-of-friend algorithm is applied to luminous galaxies using a linking length of 0.5 Mpc in the transverse separation and a photometric redshift difference within  $3\sigma$  along the line-of-sight direction. The center is assumed to be the position of the BCG, identified from a global BCG sample, as the brightest galaxy physically linked to the candidate cluster. In a similar fashion to the AMF catalog, the richness is computed from the total luminosity of all galaxies brighter than  $0.4L_*$ , in units of  $L_*$ . The sample is limited to a richness threshold of 12. The algorithm was applied to the latest SDSS-III data release, resulting in an increase of factor two in area. With a larger overlap with BOSS, especially in the south Galactic region, we obtain 15112 clusters within one degree off the edge of the background BOSS sample. In the following, this sample will be referred to as “WHL12”, and the richness denoted  $\Lambda_{200}$  for consistency with the notation adopted for the AMF catalog.

Finally, we complete our set of foreground cluster catalogs with the meta-catalogue of X-ray detected clusters (MCXC) assembled by Piffaretti et al. (2011). This data set is a compilation of X-ray detected clusters from a number of publicly available data collected by the ROSAT satellite. The sample extends to redshift  $\sim 0.6$  with a wide range of masses. Here we relax the maximum redshift range to  $z = 0.35$  as the majority of clusters have secure spectroscopic redshift measurements and do not suffer from false detection caused by projection effects.

The number of clusters in common over the DR9 (see below) released BOSS area is currently 158.

## 2.2. The Source Sample

Our background sample is extracted from the first data release “DR9” of the BOSS spectroscopic survey. BOSS aims at measuring the scale of baryon acoustic oscillations at redshift  $z = 0.5$  as a sensitive cosmological test. The first data release, covering  $3000 \text{ deg}^2$ , was made publicly available in summer 2012 through the SDSS III/BOSS DR9 data release<sup>5</sup>.

We use the “CMASS” spectroscopic sample for which the targets were selected in the range  $17.5 < i_{AB} < 19.9$ , using color selection techniques to ensure homogeneous sample in mass between redshifts 0.43 and 0.7. We refer to Maraston et al. (2012) for a complete study of the galaxy stellar mass function and the verification of the homogeneity of the data across the full redshift range.

The BOSS DR9 data release comprises about  $3000 \text{ deg}^2$  in the south and north galactic areas. We further select only primary spectroscopic galaxies, and remove all galaxies with uncertain redshift measurements, by imposing the flag `zwarning=0`. The total number of galaxies used as background sources is 316220.

Fig. 1 illustrates the data coverage used in this study. The foreground cluster sample is shown in blue and the background BOSS galaxy sample in red. We show the maxBCG clusters as an example, and note that the WHL12 sample has a better overlap with BOSS in the south Galactic part. The two other catalogues have a similar coverage compared to maxBCG, and the MCXC has a full coverage over the BOSS area but is not spatially homogeneous because it is drawn from several independent X-ray surveys. We summarize in Table 1 cluster sample properties.

## 3. MODEL

In this section we outline the formalism that describes the systematic effect of lens magnification modifying the source selection function, by foreground galaxy clusters. Lensing magnification is caused by both isotropic and anisotropic focusing of light rays due to the presence of massive foreground objects acting as gravitational lenses. The former effect is described by the convergence,  $\kappa(r) = \Sigma(r)/\Sigma_{\text{crit}}$ , the projected mass density  $\Sigma(r)$  in units of the critical surface mass density,

$$\Sigma_{\text{crit}} = \frac{c^2}{4\pi G} \frac{D_s}{D_l D_{ls}}, \quad (1)$$

where  $D_l$ ,  $D_s$ , and  $D_{ls}$  are the proper angular diameter distances from the observer to the lens, the observer to the source, and the lens to the source. The latter effect is due to the gravitational shear  $\gamma(r) = \gamma_1 + i\gamma_2$  with spin-2 rotational symmetry (see Bartelmann & Schneider 2001).

Since gravitational lensing conserves surface brightness, the apparent flux of background sources increases in proportion to the magnification factor. This shift in magnitude implies that the limiting luminosity at any background redshift lies effectively at a fainter limit given by  $L_{\text{lim}}(z)/\mu(z)$ , hence increasing the surface density

<sup>5</sup> [http://www.sdss3.org/dr9/data\\_access/](http://www.sdss3.org/dr9/data_access/)

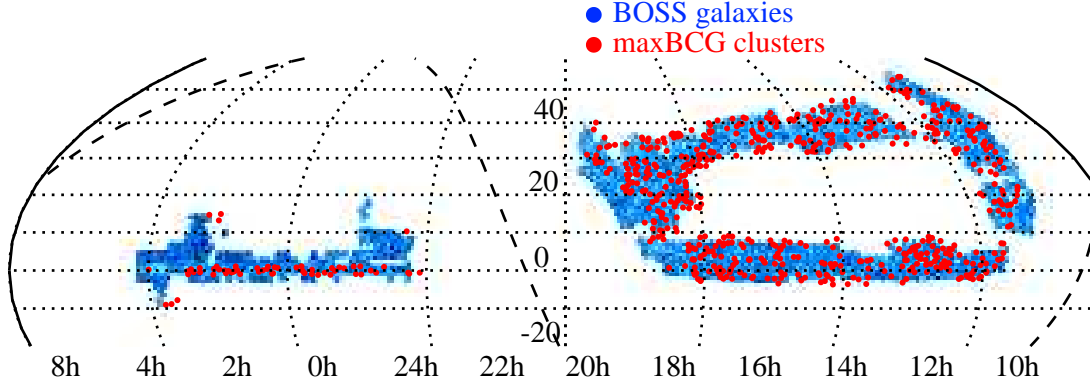


**Figure 1.** Data coverage of BOSS galaxies (blue) and maxBCG clusters (red) in equatorial coordinates. We only display the clusters selected to be within one deg of BOSS area used in this study. The dashed line is the Galactic equatorial plane.

of magnified sources behind foreground lenses. On the other hand, the number of background sources per unit area decreases due to the expansion of sky area. These two effects compete with each other, and the effective variation in the source number density  $n_{\text{eff}}$ , known as the magnification bias (BTP95), depends on the steepness of the source number counts as a function of the flux limit  $F$ .

For background sources at redshift  $z$ , the magnification bias is expressed as

$$n_{\text{eff}}[> F(z)] = \frac{1}{\mu(z)} n_0 \left[ > \frac{F(z)}{\mu(z)} \right], \quad (2)$$

where  $n_0$  is the unlensed number density of background sources,  $L$  the limiting luminosity of the background sample, and  $\mu$  the magnification,

$$\mu = \frac{1}{(1 - \kappa)^2 - |\gamma|^2}. \quad (3)$$

For the case of weak gravitational lensing, the magnitude shift induced by magnification is sufficiently small, so that the source number count can be locally approximated by a power law at the limiting luminosity. This simplifies Eq. 2 to

$$n_{\text{eff}}(z) = \mu^{\beta(z, L) - 1} n_0(z), \quad (4)$$

with  $\beta$  the logarithmic slope of the luminosity function  $\Phi$  evaluated at the limiting luminosity:

$$\beta(z, L) = - \left. \frac{d \ln \Phi[L', z]}{d \ln L'} \right|_L. \quad (5)$$

We retrieve the well-known result that if the count slope  $\beta(z, L)$  is greater than unity, the net effect of magnification bias is to increase the source number density, or decrease otherwise (BTP95). If the count slope is unity, the net magnification effect on the source counts vanishes. In the strict weak-lensing limit, the magnification bias is directly related to the projected mass distribution

as  $n_{\text{eff}}(z)/n_0(z) \approx 2[\beta(z, L) - 1]\kappa(z)$ .<sup>6</sup>

The limiting magnitude and the count slope vary with redshift, so that the integrated magnification-bias effect will translate into an enhancement in mean source redshift as

$$\bar{z}_{\text{lensed}} = \frac{\int n_{\text{eff}}(z) z dz}{\int n_{\text{eff}}(z) dz}. \quad (6)$$

The limiting luminosity can be computed from the apparent limiting magnitude for a given survey as

$$-2.5 \log_{10} L(z) = i_{\text{AB}} - 5 \log_{10} \frac{d_L(z)}{10 \text{ pc}} - K(z) \quad (7)$$

where  $i_{\text{AB}} = 19.9$  is the limiting magnitude of BOSS,  $d_L$  the luminosity distance, and  $K$ , the  $K$ -correction:

$$K(z) = 2.5(1 + z) + 2.5 \log_{10} \left[ \frac{L(\lambda_e)}{L(\lambda_0)} \right]. \quad (8)$$

In our analysis, we restrict the source redshift range to  $0.43 < z < 0.7$ , where the BOSS target selection is established to be uniform (Dawson et al. 2013). We assume a Schechter (1976) luminosity function with the parameters measured in the VIMOS VLT Deep Survey (VVDS, Le Fèvre et al. 2005) by Ilbert et al. (2005). The authors provide a detailed measurement of the luminosity function in all  $UBVRI$  optical bands of the survey over a wide redshift range,  $0.2 < z < 2.0$ . This survey has the advantage of being considerably deeper than the BOSS survey, with redshift completeness to a fainter limiting magnitude and therefore describes better the underlying luminosity function, in terms of the slope as a function of redshift and magnitude required here for our lensing predictions. To minimize the uncertainties on the  $K$ -correction, we take the rest-frame  $V$ -band luminosity function measured at redshift  $\sim 0.5$ , which best matches the redshifted galaxies observed in the  $i$ -band at redshift

<sup>6</sup> In the present analysis, we have used the full expression without the weak-lensing approximation.

0.5, so that this choice allows us to neglect the second term in Eq. 8.

Finally, to account for luminosity evolution as function of redshift, we employed the parametrization of Faber et al. (2007), such that our assumed Schechter parameters are:

$$M_* = -22.27 - 1.23 \times (z - 0.5) \quad (9)$$

$$\alpha = -1.35. \quad (10)$$

Note that no precise normalization of the luminosity function is required for our analysis but only the gradient of the logarithmic slope  $\beta$  at the limiting luminosity as a function of background redshift, which has been well determined from the VVDS, and confirmed by other deep probes of similar volume such as the COMBO-17 photometric survey (Wolf et al. 2003) or DEEP2 spectroscopic survey (Willmer et al. 2006). In particular, the  $M_*$  parameter measured in the  $B$ -band is found to be in excellent agreement among those three deep surveys at  $z = 0.5$  (Faber et al. 2007, Fig. 7).

The VVDS field-of-view is one deg<sup>2</sup>, comprising 11 034 redshift measurements, allowing us to determine the respective levels of Poisson uncertainty and cosmic variance into the Schechter parameters we require for our predictions. We quantify in Sec. 6.6 the impact of these assumptions on the size of the mean redshift depth enhancement predicted. In particular we show that these model uncertainties arising from the parameterisation of the luminosity function are substantial compared to the detected signal, however smaller than our statistical errors on the measurements from the current DR9 release.

To date, a number of studies (Umetsu et al. 2011b; Hildebrandt et al. 2011; Ford et al. 2012) have measured a magnification-bias signal by assuming an effective single-plane source redshift for a given background sample and comparing their number density to a random sample. Here we do not need to approximate the depth as we have precise spectroscopic redshift measurements for all individual sources, providing a direct estimate for the enhancement of mean source redshift behind clusters with respect to that of the total sample.

Our method developed here has two main advantages over the standard magnification-bias because we are simply measuring an averaged depth enhancement of the background galaxies, rather than the lensing induced change in the surface density of galaxies. The latter effect requires careful correction for screening by foreground/cluster galaxies. Secondly, since we probe a relatively narrow redshift range of galaxies having a well-understood selection function than for typical faint background source counts used in the magnification bias work located at  $z \sim 1 - 3$ . Therefore, our method enables in practice a relatively better understood determination of the statistical lensing effect for the foreground clusters we are examining.

To quantify and characterize the cluster mass distribution, we compare the observed cluster lensing profiles with analytic spherical halo density profiles. In the present study, we consider (1) the Navarro et al. (1997, hereafter NFW) and (2) the singular isothermal sphere (SIS) models. The former is a theoretically- and observationally-motivated model of the internal structure of cluster-sized halos (e.g. Okabe et al. 2010;

Umetsu et al. 2011a),  $\rho(r) \propto (r/r_s)^{-1}(1 + r/r_s)^{-2}$  with  $r_s$  the characteristic radius at which the logarithmic density slope is isothermal. The latter model provides a simple, one-parameter description of isothermal density profiles,  $\rho(r) \propto r^{-2}$ .

The two-parameter NFW model can be specified by the degree of concentration,  $c_{200} = r_{200}/r_s$ , and the halo mass,

$$M_{200} = \frac{4\pi}{3} 200 \rho_{\text{crit}}(z) r_{200}^3, \quad (11)$$

the total mass enclosed within a sphere of radius  $r_{200}$ , within which the mean interior density is 200 times the critical mass density at the cluster redshift,  $\rho_{\text{crit}}(z)$ . Here we employ the mean concentration-mass relation of Bhattacharya et al. (2013), derived from  $\Lambda$ CDM cosmological  $N$ -body simulations covering a wide halo mass range of  $2 \times 10^{12} - 2 \times 10^{15} M_\odot h^{-1}$  and a wide redshift range of  $z = 0 - 2$ . We use their fitting formula for the full-sample relation  $c_{200}(M_{200}, z)$ . The NFW profile is thus specified by  $M_{200}$  alone. The use of the Bhattacharya et al. (2013) relation is motivated by recent detailed cluster lensing work (Coe et al. 2012; Umetsu et al. 2012; Okabe et al. 2013) finding a good agreement with their predictions for high-mass clusters ( $M_{200} \sim 10^{15} M_\odot$ ) at  $z = 0.2 - 0.4$ . We employ the radial dependence of the projected NFW lensing profiles given by Wright & Brainerd (2000).

For the SIS model, the magnification is given by

$$\mu_{\text{SIS}}(\theta) = \frac{1}{1 - \theta_E/\theta}, \quad (12)$$

with  $\theta_E = 4\pi(\sigma_v/c)^2 D_{ls}/D_s$  the Einstein radius. Here,  $\sigma_v$  is the one-dimensional velocity dispersion related to the halo mass,

$$\sigma_v = \left[ \frac{\pi}{6} 200 \rho_{\text{crit}}(z) M_{200}^2 G^3 \right]^{1/6}. \quad (13)$$

Finally, the magnification factor is plugged into Eqs. 4 and 5, so that the depth magnification is computed as a function of the physical distance at the cluster redshift as

$$\delta_z(r) = \frac{\bar{z}(r)}{\bar{z}_{\text{total}}} - 1. \quad (14)$$

The total effect of magnification on the redshift distribution  $n(z)$  of BOSS source galaxies is shown in Fig. 2.

#### 4. MEASUREMENTS

Given the sparse source density around foreground clusters, we must measure the signal around stacked clusters to increase the signal-to-noise ratio.

To ease the computation of the mean redshift of BOSS galaxies around clusters, we employed a modified version of the Davis & Peebles (1983) two-point cross-correlation estimator:

$$w(r) = A \frac{LS}{LR} - 1 \quad (15)$$

where  $L$  is the lens cluster sample,  $S$  the source BOSS galaxy sample weighted by their redshift and  $R$  the unweighted BOSS galaxy sample. Pairs are computed at the redshift of the cluster as function of physical scale.

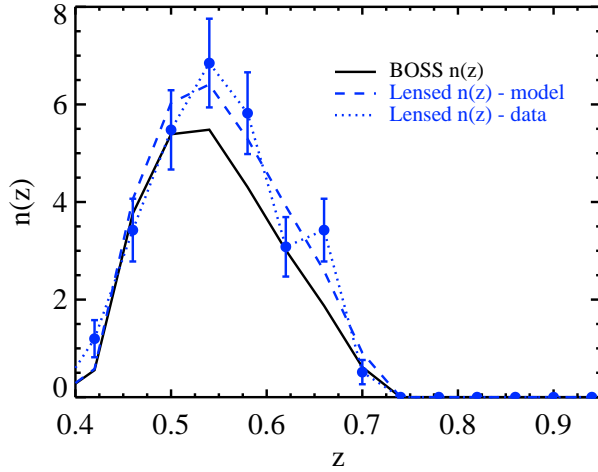


**Figure 2.** Redshift distribution of BOSS background galaxies lensed by foreground SDSS clusters (in blue: dashed line for our model; dotted line with error bars for the AMF measurements) compared to the unlensed distribution (black solid line). The model assumes an effective cluster mass of  $M_{200} = 1.81 \times 10^{14} M_{\odot}$  at  $z = 0.2$ . The observed enhancement in mean source redshift is  $\delta z \sim 0.01$ .

We can write the previous equation explicitly:

$$LS(r) = \sum_{i=1, j=1}^{n_l(r), n_s(r)} 1 \times z_j \quad (16)$$

$$LR(r) = n_l(r) \times n_s(r) \quad (17)$$

so that

$$\frac{LS}{LR}(r) = \bar{z}(r) \quad (18)$$

and

$$A^{-1} = \frac{1}{N_l} \sum_{i=1, j=1}^{N_l, N_s} 1 \times z_j = \bar{z}_{\text{total}}, \quad (19)$$

where the subscripts  $l$  and  $s$  denote the lens and source samples, respectively. Equation 15 then reduces to

$$w(r) = \frac{\bar{z}(r)}{\bar{z}_{\text{total}}} - 1 \equiv \delta_z(r), \quad (20)$$

as defined by Eq. 14.

In practice we perform the measurements using the software SWOT (Coupon et al. 2012), a fast two-point correlation code optimized for large data sets. The algorithm makes use of large scale approximations, tree-code structured data, and parallel computing to considerably accelerate pair counting. Correlating  $\sim 300\,000$  background objects with  $\sim 6\,000$  foreground objects takes about five minutes on a desktop computer.

Error bars are estimated by generating foreground cluster positions over the BOSS area: using 20 000 points with random projected positions on the sky and a volume-weighted random redshift in the range  $0.1 < z < 0.3$ , we compute  $w(r)$  in a similar fashion as for the data samples, using the same binning. We repeat the process 100 times and compute the dispersion of the ensemble. Error bars for the signal of each cluster sample

are further multiplied by  $\sqrt{20\,000/N_{\text{clusters}}}$  to account for Poisson error. Additionally, the significance of the detection for each sample is computed using the rescaled covariance matrix.

For optically detected cluster samples, we compare our measurements to the expected theoretical signal by first converting the richness to the mass, using the maxBCG mass-richness relationship calibrated from X-ray and weak lensing by Rozo et al. (2009):

$$\frac{M_{500}}{10^{14} M_{\odot}} = \exp(0.95) \left( \frac{N_{200}}{40} \right)^{1.06}, \quad (21)$$

and we further convert  $M_{500}$  into  $M_{200}$  using the method described in Hu & Kravtsov (2003), and the concentration-mass relationship of Bhattacharya et al. (2013). We employ the same relation for GMBCG, as the richness definition is identical to maxBCG.

As for the WHL12 sample, the authors chose a different definition for the richness (see Sec. 2.1), but also provide an independent X-ray/lensing calibrated mass-richness relationship (Wen et al. 2010):

$$\frac{M_{200}}{10^{14} M_{\odot}} = 10^{-1.49} \Lambda_{200}^{1.17}. \quad (22)$$

Since the richness definition assumed for AMF is similar to that of WHL12 we use the same parametrisation for these two samples.

For the X-ray cluster sample, an estimation of the  $M_{500}$  mass is directly provided, however due to the low angular resolution of ROSAT, X-ray mass estimates may be underestimated. To correct for this, we matched the MCXC clusters with the local cluster sample presented in Vikhlinin et al. (2009), and compared the value of  $M_{500}$ :

$$M'_{500} = 10^{-0.951} M_{500}^{1.067}. \quad (23)$$

Then we simply convert  $M'_{500}$  into  $M_{200}$  as described above. It is found that the MCXC-based value is about 25% smaller than those derived by Vikhlinin et al. (2009) at the effective mass of our subsample  $M_{200} \sim 5 \times 10^{14} M_{\odot}$ .

Finally to perform a strict comparison between the stacked measured signal and the prediction, we compute the composite halo-mass theoretical signal:

$$\delta_z(r) = \frac{1}{N_l} \sum_{i=1}^{N_l} \delta_{z,i}(r, M_{200}). \quad (24)$$

## 5. RESULTS

We show in Fig. 3 our measurements for the four maxBCG, GMBCG, AMF, and WHL12 SDSS cluster samples. Similarly, Fig. 4 shows our results for the X-ray MCXC cluster sample.

As described in Sec. 4, the errors are obtained from the standard deviation of 100 subsamples with 20 000 randomized cluster positions over the BOSS area, and rescaled for each individual sample depending on the number of clusters to account for Poisson uncertainty. The detection significance, shown in Table 1 for each individual sample, is computed for all data points with 10 cluster-galaxy pairs or more, using the covariance matrix of the random samples up to  $r = 10.0$  Mpc. The resulting covariance matrix is displayed in Fig. 5: the higher

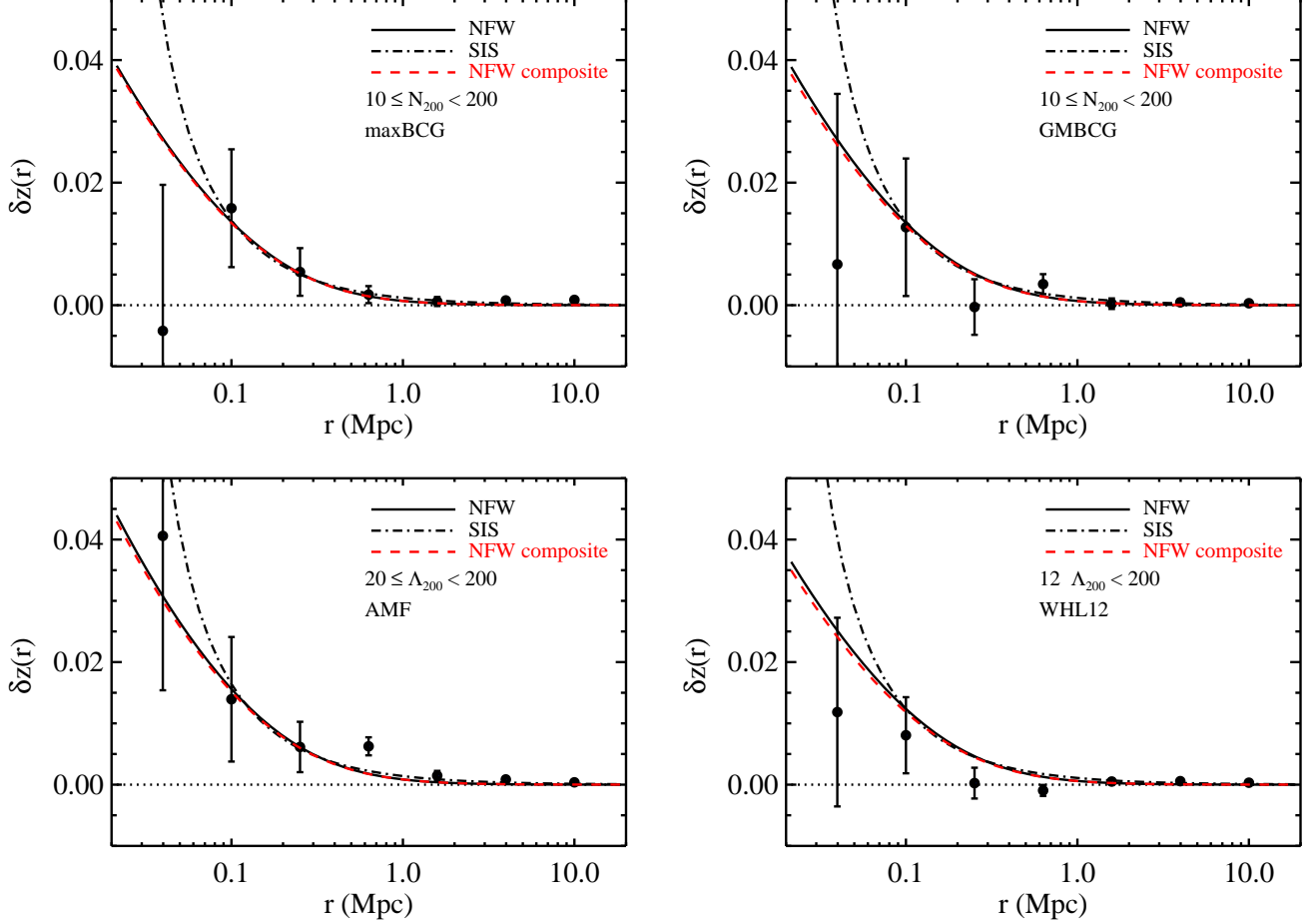


**Figure 3.** Mean redshift increase of BOSS galaxies measured around SDSS clusters from the maxBCG (top left), GMBCG (top right), AMF (bottom left), and WHL12 (bottom right) samples. The red dashed (composite) and black solid lines are NFW profile predictions assuming a mass-richness relationship calibrated from X-ray and weak lensing measurements taken from the literature. We also show the SIS profile prediction (dotted dashed line). Error bars were computed by calculating the background mean redshifts radially around 20,000 randomized foreground positions over the BOSS area and normalised to the cluster sample size.

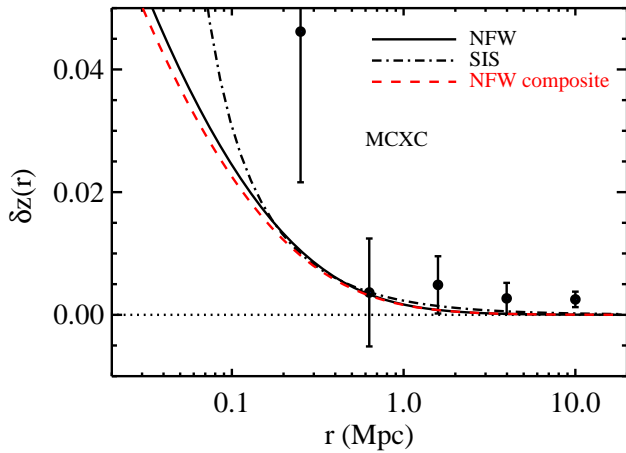


**Figure 4.** Same as Fig. 3, but for the X-ray MCXC sample.

correlation at large scales translates into the fact that the same background galaxy may be used for several cluster-galaxy pairs. On the other hand, there is little correlation

at smaller scales ( $< 1$  Mpc) due to the relatively sparse distribution of foreground clusters (approximately, two per sq. deg).

For each case, the red-dashed line represents the composite-NFW lensing signal expected for the respective cluster sample, obtained assuming a mass-richness relationship calibrated from X-ray and weak-lensing measurements taken from the published literature: given by Rozo et al. (2009) for maxBCG and GMBG (Eq. 21) and by Wen et al. (2012) for AMF and WHL12 (Eq. 24), whereas the  $M_{200}$  masses for MCXC have been translated from their  $M_{500}$  values assuming the NFW form.

For comparison, we also plot the expected lensing signal obtained assuming a single effective mass ( $M_{200}$ ), for the NFW (black solid line) and SIS (black-dotted dashed line) profiles. At small scales, there is a small difference between the composite versus single NFW profiles, which however is not significant due to the large statistical errors. As for the SIS case, overall, it is likely that the lensing signal at small scales is overestimated. Here, it is reassuring to see that the NFW model provides a better description of the observed lensing signals because the lensing-based mass-richness relationships were calibrated



**Table 1**  
Properties of cluster samples.

Sample	$N_{\text{clusters}}$	Effective $M_{200}$ mass [ $\times 10^{14} M_{\odot}$ ]	Redshift	Detection method	Significance ( $\sigma$ )	Reference
maxBCG	6 308	1.48	$0.1 < z < 0.3$	red sequence	4.8	1
GMBCG	4 631	1.40	$0.1 < z < 0.3$	red sequence + BCG	2.8	2
AMF	5 646	1.81	$0.1 < z < 0.3$	aperture matched filter	4.9	3
WHJ12	15 112	1.18	$0.1 < z < 0.3$	photo-z	3.5	4
MCXC	158	5.00	$0.1 < z < 0.35$	X-ray	2.8	5

**References.** — (1) Koester et al. (2007); (2) Hao et al. (2010); (3) Szabo et al. (2011); (4) Wen et al. (2012) ; (5) Piffaretti et al. (2011).

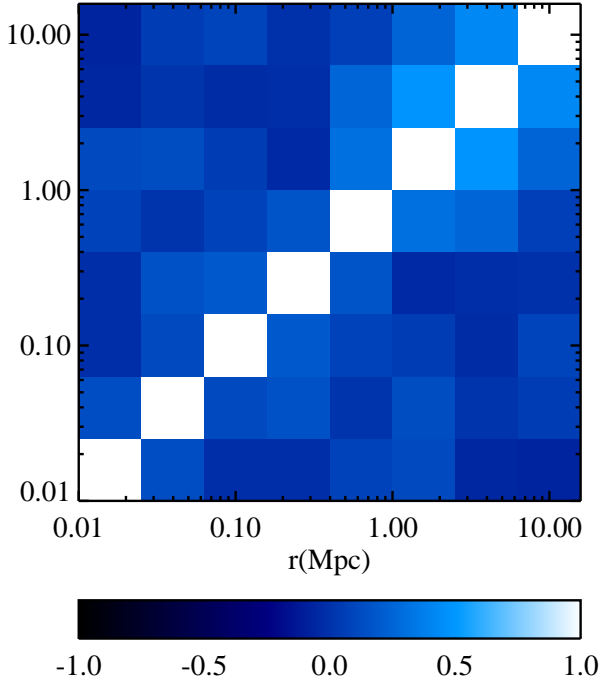


**Figure 5.** Correlation matrix of the covariance matrix estimated from the 100 subsamples with randomized cluster positions in the BOSS area. The result shown here was computed using 20,000 random points for each of the 100 subsamples.

assuming the NFW form in all cases for the maxBCG relation (Johnston et al. 2007; Mandelbaum et al. 2008; Sheldon et al. 2009), and most cases for the WHL12 relation (Wen et al. 2010, and references therein).

These results demonstrate the robustness of our measurements and appear to be in excellent agreement with previous lensing studies. Although the large statistical errors prevent us from accurately testing both the amplitude and slope of the mass-richness relationship for the current BOSS sample, it is interesting to compare the results between the different cluster samples. With a detection significance at the nearly  $5\sigma$  level, the maxBCG and AMF samples seem to give the highest-confidence detections among our cluster samples. The AMF catalog catalogue has the highest minimum richness cut ( $\Lambda_{200} \geq 20$ ) but the averaged signal appears to be relatively higher so that the lower number of clusters above this richness cut is almost compensated by a greater lensing signal due to their higher cluster masses.

On the other hand, the measured lensing signal in the WHL12 sample is shown to be relatively low compared to the model prediction based on the same mass-richness relationship, despite its larger sample size and greater overlap with current BOSS sky area. This could be a consequence of a relatively higher impurity of the cluster sample, due perhaps to a higher rate of false detections, which will lead to an underestimation of the geometric lensing signal as found here. Similarly, we obtained for GMBCG a relatively low level of detection significance,  $2.4\sigma$ . It is interesting to note that Wen et al. (2012) find a lower matching rate of their WHL12 clusters with GMBCG, compared to that with maxBCG. This could indicate that these two samples have a higher level of contamination by false cluster detections. Another interesting point is that the cluster redshift scatter between WHL12 and GMBCG can be as high as several times the photometric redshift errors, as shown by their comparison (Wen et al. 2012, Table 8). A more detailed and careful analysis would be certainly required to confirm such a conclusion. We shall come back to this issue and its consequence for magnification bias contamination in Sec. 6.4.

The MCXC X-ray sample has the largest statistical errors due to the small number, 158, of clusters (Fig. 4). However, it is worth noting that there is a likely excess of the lensing signal at  $r \simeq 2\text{--}10\text{ Mpc}$  ( $> r_{200}$ ) with respect to the NFW predictions, which cannot be explained by simply increasing the halo masses. In the context of  $\Lambda\text{CDM}$ , this large-scale excess signal can be naturally explained by the two-halo term contribution due to large-scale structure associated with the central clusters (see Oguri & Hamana 2011). We note that, in contrast to the gravitational shear, magnification is sensitive to the sheet-like mass distribution, and therefore can be used as a powerful tool to probe the two-halo term in projection space.

## 6. ERROR ANALYSIS

### 6.1. Sources Sample Variance

As described in Sec. 4, our error estimate simply reflects the statistical variation of the mean redshift of sources across the BOSS area. This estimator primarily provides a measure of the source sample variance given a sample of foreground clusters, because it measures the fluctuations of the number counts across the field. We display the magnification signal as measured for AMF (for which we find the highest level of detection significance) in the top panel of Fig. 6, compared to the mean signal from the random samples shown in the bottom panel. The random-sample signal is consistent with null



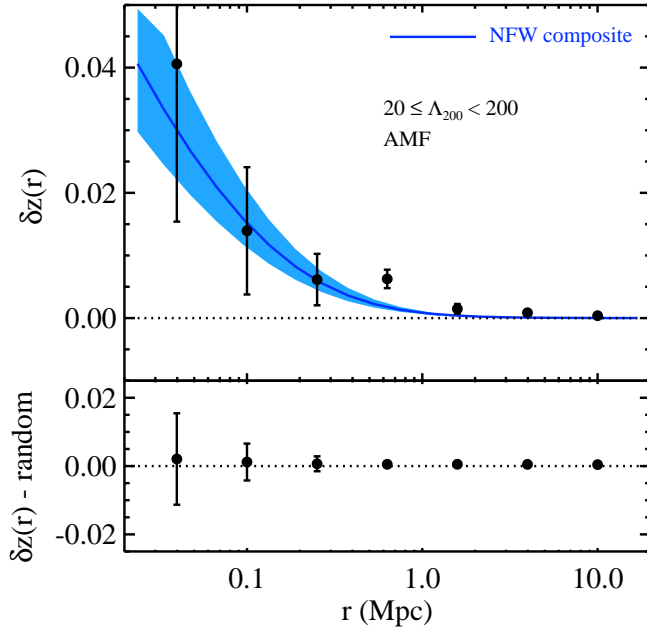


**Figure 6.** Measured signal for the AMF sample (top) compared to the mean signal around random positions drawn in the BOSS area (bottom). The error bars show the dispersion for 100 samples with randomised cluster positions, mainly accounting for the source sample variance around the cluster sample. In blue we display the expected NFW signal as in Fig.3, where the shaded area represents an estimate on our model uncertainties due to the assumptions on the luminosity function.

detection, indicating that the 100 random samples are sufficiently large for realistic estimates of the errors.

### 6.2. Spectroscopic Redshift Errors

The errors on individual source redshifts might also affect our statistical lensing measurements if only a small number of cluster-galaxy pairs are used at small scales ( $\lesssim 0.05$  Mpc). However, the mean spectroscopic error is  $\Delta z = 1.3 \times 10^{-4}$ , so that our measured signal is two orders of magnitude larger than that. Hence, we conclude that this should not have a significant impact on our measurements.

### 6.3. Photometric Calibration

The primary requirement of our analysis method is an homogeneous target selection across the survey field. In particular, a spatial variation of the photometric calibration would affect both the cluster detections and the BOSS target selection. In our analysis, we can rely on the accurate and homogeneous calibration of the SDSS data (Fukugita et al. 1996; Gunn et al. 1998). We have checked that a variation of a few 0.01 magnitude would cause a mean redshift change less than  $\delta z = 5 \times 10^{-4}$ , which is again significantly smaller than the measured signal.

### 6.4. False Cluster Detections

Perhaps the most important source of systematics in magnification bias methods originates from the potential contamination by physically associated lens-source

pairs that create a spurious correlation signal indistinguishable from the lensing signal. Since we use spectroscopic redshift information for the background, low-redshift contamination by background sources can be neglected here. Hence, the only possible source for such systematics would arise from erroneously-detected distant clusters. Let us consider a galaxy overdensity (such as rich clusters or filamentary structure) located in the source range  $0.43 < z < 0.7$  whose member galaxies were misattributed to foreground galaxies with lower photometric redshifts, which can be incorrectly detected as a low redshift cluster. Since cluster-sized overdensities can have a significant impact on the redshift distribution, the resulting mean redshift could be noticeably different from that of the whole sample.

The maxBCG and GMBCG samples would have the lowest chance of being affected by this effect, because their detection algorithms rely on bright red galaxies, for which we expect a very low rate of photometric redshift outliers (defined as being off by a few sigmas) due to a clear measurable Balmer break in the redshift range considered here, and the high rate of spectroscopic redshifts for these objects. On the other hand, for the WHL12 and AMF samples which make use of the full galaxy population with photometric redshifts, such misidentification is more likely to happen.

Interestingly, Fig. 4 in Oyaizu et al. (2008) shows a photometric-to-spectroscopic redshift comparison of the CC2 sample that was used for AMF. A closer look at the published figure suggests that very few galaxies (one can count only six galaxies out of  $\sim 10\,000$  – less than 0.1%) scatter from the redshift range  $[0.43 : 0.7]$  to  $[0.1 : 0.3]$ . Taking into account the increased scatter in overdense regions, a threshold richness of  $\sim 10$  in cluster catalogs implies that only those clusters which are richer than a few hundreds would be large enough to cause such a false detection at low redshift.

Also rare, but more likely to occur than in the previous case, is massive filaments aligned with the line-of-sight, which can lead to enhanced low- $z$  contamination. This might cause a false cluster detection *and* also impact the mean redshift estimation of the background sample. Again from Fig. 4 in Oyaizu et al. (2008), it is clearly seen that the scattered galaxies lie below the mean redshift of BOSS galaxies. This means that the expected direction of this effect would be to decrease the mean redshift and bias low our measurements. This could constitute a plausible explanation for the low signal level measured from WHL12, since they employ photometric redshifts in their detection algorithm.

It is worth noting that such large overdensities would be easy to spot and mask out in a spectroscopic background sample, when the statistical significance of the BOSS survey improves.

### 6.5. Cluster Miscentering

Misidentification of cluster centers is another potential source of systematic errors for cluster lensing measurements at small scales. Recently, George et al. (2012) studied the impact of the choice for the cluster center on the measured lensing signal based on X-ray galaxy groups detected in the COSMOS field. Their findings show that at small scales ( $< 0.1$  Mpc), choosing the BCG over the most massive galaxy close to the X-ray peak position

(their center definition yielding the best result) reduces the signal by about 20% within 75 Kpc.

Johnston et al. (2007) demonstrated that the lensing convergence  $\kappa$ , which is locally related to the magnification to first order, is less affected by cluster miscentering than the weak shear, and that smoothing due to miscentering effects nearly vanishes at twice the typical positional offset from the cluster mass centroid. This indicates that our results would not be affected by the miscentering effects beyond a radius of  $r = 0.15$  Mpc. In our present analysis, the statistical uncertainty is too large to be able to estimate the degree of miscentering or the likely level of correction from our data. Still, it is worth noting that our measurements show the lensing signal decreases at small scales for three out of the four samples, although these cluster samples are not entirely independent with sizeable proportions of clusters in common (Wen et al. 2012).

### 6.6. Model Uncertainties

In this work, while we attempt to demonstrate the feasibility and great potential of this new method, we are limited by statistical uncertainties and thus unable to constrain both the amplitude and slope of the mass-richness relationship. When BOSS is completed, it will increase the respective size of background sample and the large area of sky covered – which means we can also increase the size of the foreground cluster samples by a factor of three – leading to an anticipated factor-three increase in the signal-to-noise ratio. This will then allow us to subdivide cluster samples into bins of richness, thus complementing the standard shear-based mass measurements. A further substantial improvement is expected in near future with bigBOSS and the NIR spectroscopic survey of EUCLID, which will increase the sample size of background galaxies by one order of magnitude. More importantly, EUCLID will obtain a sufficiently large number of spectra of background sources at  $z > 1$ , pushing the foreground cluster sample to higher redshift than shear measurement will allow. Similarly, the ambitious Subaru Prime Focus Spectrograph (PFS, Sugai et al. 2012) survey with its powerful NIR capability promises to provide an unprecedented large high-redshift sample of spectroscopic redshifts.

To fully exploit the greater statistical power in future surveys, it is critical to control systematics. In particular, the luminosity function slopes of source samples must be precisely known, in order to accurately extract the lensing signal from observations. To do this, a homogeneous selection of background sources is crucial.

To compute theoretical predictions, we have implicitly assumed that mass is proportional to luminosity when constructing the above composite cluster lensing mass profiles. In details we must expect that the mass-to-light ratio varies as a function of mass, redshift, and galaxy type. In Coupon et al. (2012), we fit the mass-to-light ratio as function of mass and redshift for blue and red galaxies, using the 30-band COSMOS data (Ilbert et al. 2009): in the mass bin  $10^{10.5} - 10^{11.5} M_{\odot}$ , we find the slope of the luminosity function changes from 0.44 to 0.69 depending of the galaxy type. This implies that, at most, the change in luminosity keeping a constant mass would be about 0.1 magnitude from redshift 0.4 to 0.7. Given the parametrization of the luminosity function employed

here we can test how the slope of the number counts would be affected by simply shifting the limiting magnitude by 0.1. In practice, since we are concerned only with the relatively bright end of the galaxy distribution, it is equivalent to a shift in  $M_{\star}$  parameter.

Furthermore, two additional sources of systematic errors could have affected the determination of the source luminosity function by Ilbert et al. (2005): the Poisson error and the cosmic variance. The former was estimated by Ilbert et al. (2005), and given as  $\Delta M_{\star} \sim 0.25$ , which is correlated with the faint-end slope  $\alpha$ , so that this estimate may be rather pessimistic. For the later, the effect of cosmic variance on the count slope is more difficult to assess. To obtain a crude estimate of this effect we consider the value of  $\Delta M_{\star} = 0.02$ , which was estimated by Loveday et al. (2012) for the GAMA survey from jack-knife resampling of nine subregions each with  $16 \text{ deg}^2$ . Although GAMA is a lower-redshift survey compared to VVDS, the volume of each subregion is larger than the volume probed over the  $1 \text{ deg}^2$  field-of-view of VVDS at  $z = 0.5$ , so that we have adopted a conservative estimate of 0.1.

Finally we add in quadrature all three sources of systematic uncertainty, and reexamine our model predictions in the two extreme cases,  $M_{\star} \pm 0.29$ . In Fig. 6, the resulting error region is indicated by the blue-shaded area which is systematically less than the statistical error for the current dataset.

## 7. CONCLUSIONS

Using over 300 000 BOSS galaxies we have measured the mean redshift of background galaxies behind large samples of SDSS galaxy clusters. Our results show a net increase of the mean redshift behind the clusters compared to that of the total sample, in line with reasonable expectations for the effect of lens magnification. We have tested four different cluster catalogs, the maxBCG, GMBCG, AMF and WHL12 samples, with detection significance ranging from  $2.8\sigma$  (GMBCG) to  $4.9\sigma$  (AMF), where the level of systematic errors is expected to be negligible compared to our statistical errors. In order to speed-up and ease the measurements of the mean redshift as function of physical scale around clusters, we employed a sophisticated code (SWOT) that performs rapid parallel calculations and accurate error estimations, making practical the handling of future samples containing several millions of objects.

Based on precise measurements of luminosity functions from a number of deep spectroscopic surveys, and on an accurate modelling of dark matter halo profiles, we have compared our results to theoretical predictions. We constructed the expected signal by summing the individual contribution for each cluster given its richness from two independently established mass-richness relationships corresponding to two kinds of richness definition, and each calibrated with X-ray and weak lensing data. For three samples out of four, the agreement with the NFW profile is excellent. The mean masses of the clusters derived from our basic stacking analysis vary between the four large SDSS cluster samples in the range  $1.18\text{--}1.81^{+0.14}_{-0.14} M_{\odot}$ , after allowing for the mass-richness relations appropriate for each cluster sample and with a mean radial profile consistent with the observed radial trend towards higher mean redshift at smaller cluster ra-

dius. Only WHL12 showed a marginal deviation from the expected level, suggesting an underestimated signal. Given the high density of candidate clusters in this catalog compared to the others, this effect may indicate a somewhat larger contamination of spurious clusters that dilute the lensing signal in proportion to the fraction of false detections.

Further investigation of possible sources of systematic error will be feasible with a more thorough understanding of the source population of the BOSS survey, in terms of colour and magnitude selection and Eddington bias affecting the very bright end of the BOSS luminosity function, arising from photometric error. With the current sample, given our relatively large statistical errors we conclude that the systematic errors in the measurements should be negligible at present but that with the completion of the BOSS survey we will reach an increased level of precision that may warrant closer scrutiny of the details of the source selection function and possible redshift uncertainties for the foreground cluster populations. We believe that the method is very robust against systematic errors, even when we increase the statistical power in future experiments such as bigBOSS, PFS and EUCLID (which will observe background sources 25 times as dense and over 5 times the area of this study) with millions of spectroscopic/grism redshifts, at which point this method will be powerful in its own right for defining cluster mass-concentration relations and the evolution of the cluster mass function. These results may be compared with independent estimates of magnification bias from faint number counts and with cosmic shear measurements for which the sources of systematic error are very different.

We acknowledge Yen-Ting Lin for fruitful discussions and comments, and for providing us with the calibration formula for MCXC masses.

Funding for SDSS-III has been provided by the Alfred P. Sloan Foundation, the Participating Institutions, the National Science Foundation, and the U.S. Department of Energy Office of Science. The SDSS-III web site is <http://www.sdss3.org/>.

SDSS-III is managed by the Astrophysical Research Consortium for the Participating Institutions of the SDSS-III Collaboration including the University of Arizona, the Brazilian Participation Group, Brookhaven National Laboratory, University of Cambridge, Carnegie Mellon University, University of Florida, the French Participation Group, the German Participation Group, Harvard University, the Instituto de Astrofísica de Canarias, the Michigan State/Notre Dame/JINA Participation Group, Johns Hopkins University, Lawrence Berkeley National Laboratory, Max Planck Institute for Astrophysics, Max Planck Institute for Extraterrestrial Physics, New Mexico State University, New York University, Ohio State University, Pennsylvania State University, University of Portsmouth, Princeton University, the Spanish Participation Group, University of Tokyo, University of Utah, Vanderbilt University, University of Virginia, University of Washington, and Yale University.

The work is partially supported by the National Science Council of Taiwan under the grant NSC97-2112-M-001-020-MY3 and by the Academia Sinica Career Devel-

opment Award.

## REFERENCES

- Bartelmann, M. & Schneider, P. 2001, *Phys. Rep.*, 340, 291  
 Benjamin, J., Van Waerbeke, L., Heymans, C., et al. 2012, *ArXiv e-prints*  
 Bhattacharya, S., Habib, S., Heitmann, K., & Vikhlinin, A. 2013, *ApJ*, 766, 32  
 Broadhurst, T., Takada, M., Umetsu, K., et al. 2005, *ApJ*, 619, L143  
 Broadhurst, T., Umetsu, K., Medezinski, E., Oguri, M., & Rephaeli, Y. 2008, *ApJ*, 685, L9  
 Broadhurst, T. J., Taylor, A. N., & Peacock, J. A. 1995, *ApJ*, 438, 49  
 Coe, D., Umetsu, K., Zitrin, A., et al. 2012, *ApJ*, 757, 22  
 Coupon, J., Kilbinger, M., McCracken, H. J., et al. 2012, *A&A*, 542, A5  
 Davis, M. & Peebles, P. J. E. 1983, *ApJ*, 267, 465  
 Dawson, K. S., Schlegel, D. J., Ahn, C. P., et al. 2013, *AJ*, 145, 10  
 Dong, F., Pierpaoli, E., Gunn, J. E., & Wechsler, R. H. 2008, *ApJ*, 676, 868  
 Faber, S. M., Willmer, C. N. A., Wolf, C., et al. 2007, *ApJ*, 665, 265  
 Ford, J., Hildebrandt, H., Van Waerbeke, L., et al. 2012, *ApJ*, 754, 143  
 Fukugita, M., Ichikawa, T., Gunn, J. E., et al. 1996, *AJ*, 111, 1748  
 George, M. R., Leauthaud, A., Bundy, K., et al. 2012, *ApJ*, 757, 2  
 Gunn, J. E., Carr, M., Rockosi, C., et al. 1998, *AJ*, 116, 3040  
 Hao, J., McKay, T. A., Koester, B. P., et al. 2010, *ApJS*, 191, 254  
 Heymans, C., Van Waerbeke, L., Miller, L., et al. 2012, *MNRAS*, 427, 146  
 Hildebrandt, H., Muzzin, A., Erben, T., et al. 2011, *ApJ*, 733, L30  
 Hildebrandt, H., van Waerbeke, L., Scott, D., et al. 2013, *MNRAS*, 429, 3230  
 Hinshaw, G., Weiland, J. L., Hill, R. S., et al. 2009, *ApJS*, 180, 225  
 Hu, W. & Kravtsov, A. V. 2003, *ApJ*, 584, 702  
 Ilbert, O., Capak, P., Salvato, M., et al. 2009, *ApJ*, 690, 1236  
 Ilbert, O., Tresse, L., Zucca, E., et al. 2005, *A&A*, 439, 863  
 Johnston, D. E., Sheldon, E. S., Tasitsiomi, A., et al. 2007, *ApJ*, 656, 27  
 Kaiser, N., Squires, G., & Broadhurst, T. 1995, *ApJ*, 449, 460  
 Kilbinger, M., Fu, L., Heymans, C., et al. 2013, *MNRAS*  
 Koester, B. P., McKay, T. A., Annis, J., et al. 2007, *ApJ*, 660, 239  
 Laureijs, R., Amiaux, J., Arduini, S., et al. 2011, *ArXiv e-prints*  
 Le Fèvre, O., Vettolani, G., Garilli, B., et al. 2005, *A&A*, 439, 845  
 Leauthaud, A., Finoguenov, A., Kneib, J.-P., et al. 2010, *ApJ*, 709, 97  
 Loveday, J., Norberg, P., Baldry, I. K., et al. 2012, *MNRAS*, 420, 1239  
 Mandelbaum, R., Seljak, U., & Hirata, C. M. 2008, *icap*, 8, 6  
 Maraston, C., Pforr, J., Henriques, B. M., et al. 2012, *ArXiv e-prints*  
 Marriage, T. A., Acquaviva, V., Ade, P. A. R., et al. 2011, *ApJ*, 737, 61  
 Massey, R., Rhodes, J., Leauthaud, A., et al. 2007, *ApJS*, 172, 239  
 Ménard, B., Scranton, R., Fukugita, M., & Richards, G. 2010, *MNRAS*, 405, 1025  
 Miller, L., Heymans, C., Kitching, T. D., et al. 2013, *MNRAS*, 429, 2858  
 Miyazaki, S., Komiyama, Y., Nakaya, H., et al. 2012, in *Society of Photo-Optical Instrumentation Engineers (SPIE) Conference Series*, Vol. 8446, *Society of Photo-Optical Instrumentation Engineers (SPIE) Conference Series*  
 More, S., van den Bosch, F. C., Cacciato, M., et al. 2011, *MNRAS*, 410, 210  
 Navarro, J. F., Frenk, C. S., & White, S. D. M. 1997, *ApJ*, 490, 493  
 Oguri, M. & Hamana, T. 2011, *MNRAS*, 414, 1851  
 Okabe, N., Smith, G. P., Umetsu, K., Takada, M., & Futamase, T. 2013, *ArXiv e-prints*  
 Okabe, N., Takada, M., Umetsu, K., Futamase, T., & Smith, G. P. 2010, *PASJ*, 62, 811  
 Oyaizu, H., Lima, M., Cunha, C. E., et al. 2008, *ApJ*, 674, 768  
 Piffaretti, R., Arnaud, M., Pratt, G. W., Pointecouteau, E., & Melin, J.-B. 2011, *A&A*, 534, A109  
 Rozo, E., Rykoff, E. S., Evrard, A., et al. 2009, *ApJ*, 699, 768  
 Rozo, E., Wechsler, R. H., Rykoff, E. S., et al. 2010, *ApJ*, 708, 645  
 Rykoff, E. S., McKay, T. A., Becker, M. R., et al. 2008, *ApJ*, 675, 1106  
 Schechter, P. 1976, *ApJ*, 203, 297  
 Schlegel, D., White, M., & Eisenstein, D. 2009, in *Astronomy, Vol. 2010, astro2010: The Astronomy and Astrophysics Decadal Survey*, 314

- Sheldon, E. S., Johnston, D. E., Scranton, R., et al. 2009, *ApJ*, 703, 2217
- Sugai, H., Karoji, H., Takato, N., et al. 2012, in *Society of Photo-Optical Instrumentation Engineers (SPIE) Conference Series*, Vol. 8446, *Society of Photo-Optical Instrumentation Engineers (SPIE) Conference Series*
- Szabo, T., Pierpaoli, E., Dong, F., Pipino, A., & Gunn, J. 2011, *ApJ*, 736, 21
- Taylor, A. N., Bacon, D. J., Gray, M. E., et al. 2004, *MNRAS*, 353, 1176
- Umetsu, K. & Broadhurst, T. 2008, *ApJ*, 684, 177
- Umetsu, K., Broadhurst, T., Zitrin, A., et al. 2011a, *ApJ*, 738, 41
- Umetsu, K., Broadhurst, T., Zitrin, A., Medezinski, E., & Hsu, L.-Y. 2011b, *ApJ*, 729, 127
- Umetsu, K., Medezinski, E., Nonino, M., et al. 2012, *ApJ*, 755, 56
- Van Waerbeke, L., Hildebrandt, H., Ford, J., & Milkeraitis, M. 2010, *ApJ*, 723, L13
- Vikhlinin, A., Burenin, R. A., Ebeling, H., et al. 2009, *ApJ*, 692, 1033
- Wen, Z. L., Han, J. L., & Liu, F. S. 2010, *MNRAS*, 407, 533
- Wen, Z. L., Han, J. L., & Liu, F. S. 2012, *ApJS*, 199, 34
- Willmer, C. N. A., Faber, S. M., Koo, D. C., et al. 2006, *ApJ*, 647, 853
- Wolf, C., Meisenheimer, K., Rix, H.-W., et al. 2003, *A&A*, 401, 73
- Wright, C. O. & Brainerd, T. G. 2000, *ApJ*, 534, 34
- York, D. G., Adelman, J., Anderson, Jr., J. E., et al. 2000, *AJ*, 120, 1579